Computer Methods and Programs in Biomedicine 226 (2022) 107154

Contents lists available at ScienceDirect

Computer Methods and Programs in Biomedicine

journal homepage: www.elsevier.com/locate/cmpb

Microstructural evaluation and recommendations for face masks in community use to reduce the transmission of respiratory infectious diseases

Alp Karakoç[a,*], Arttu Miettinen[b], Emrah Sözümert[c], Llion Evans[c], Hüseyin Yiğitler[a], Başak Bostanci[d], Ertuğrul Taciroğlu[e], Riku Jäntti[a]

[a] Aalto University, Department of Communications and Networking, Espoo, Finland
[b] Department of Physics, University of Jyväskylä, Jyväskylä, Finland
[c] College of Engineering, Swansea University, UK
[d] Institute Medicana Hospital Istanbul, Ophthalmology Department, İstanbul, Turkey
[e] University of California Los Angeles, Dept. of Civil & Environmental Engineering, USA

ARTICLE INFO

Article history:
Received 30 June 2022
Revised 12 September 2022
Accepted 21 September 2022

Keywords:
SARS-CoV-2
COVID-19
Face masks
Airborne pathogen
X-ray microtomography
Computational fluid dynamics

ABSTRACT

Background and Objective: Recommendations for the use of face masks to prevent and protect against the aerosols (≤5μm) and respiratory droplet particles (≥5μm), which can carry and transmit respiratory infections including severe acute respiratory syndrome coronavirus (SARS-CoV-2), have been in effect since the early stages of the coronavirus disease 2019 (COVID-19). The particle filtration efficiency (PFE) and air permeability are the most crucial factors affecting the level of pathogen transmission and breathability, i.e. wearer comfort, which should be investigated in detail.

Methods: In this context, this article presents a novel assessment framework for face masks combining X-ray microtomography and computational fluid dynamics simulations. In consideration to their widespread public use, two types of face masks were assessed: (I) two layer non-woven face masks and (II) the surgical masks (made out of a melt-blown fabric layer covered with two non-woven fabric layers).

Results: The results demonstrate that the surgical masks provide PFEs over 75% for particles with diameter over 0.1μm while two layer face masks are found out to have insufficient PFEs, even for the particles with diameter over 2μm (corresponding PFE is computed as 47.2%). Thus, existence of both the non-woven fabric layers for mechanical filtration and insertion of melt-blown fabric layer(s) for electrostatic filtration in the face masks were found to be highly critical to prevent the airborne pathogen transmission.

Conclusions: The present framework would assist in computational assessment of commonly used face mask types based on their microstructural characteristics including fiber diameter, orientation distributions and fiber network density. Therefore, it would be also possible to provide new yet feasible design routes for face masks to ensure reliable personal protection and optimal breathability.

1. Introduction

Since China reported a pneumonia outbreak in Wuhan, and the causative organism was identified as a new coronavirus namely, novel coronavirus: nCOV-severe acute respiratory syndrome coronavirus (SARS-CoV-2), there has been intense debate over the transmission modes of SARS-CoV-2 [1–6]. Although the World Health Organization (WHO) defined the main transmission routes of SARS-CoV-2 and its variants as direct contact, indirect contact of contaminated surfaces and inhalation of droplets from sneezing and coughing, there is growing evidence that viral transmission via aerosols is plausible under favorable conditions, particularly in closed environments with poor ventilation and long duration exposure to high concentrations of aerosols [7–9]. In the literature, droplets are accepted as particles larger than 5μm, which are sometimes visible to the human eye, produced during spitting, sneezing, and coughing. When droplets are generated they tend to settle onto surfaces and can only be removed by cleaning. On

* Corresponding author.
E-mail address: alp.karakoc@alumni.aalto.fi (A. Karakoç).

https://doi.org/10.1016/j.cmpb.2022.107154

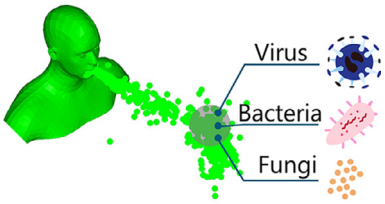

Fig. 1. Airborne pathogens carried with the respiratory particles.

the other hand, aerosols tend to be smaller than 5μm. Similar to droplets, they are generated during activities like breathing, talking and coughing [10]. The important properties of aerosols in the spread of the disease are their ability to travel long distances (7–8m from a cough), to stay in the air for more than 1 h and to be inhaled to the bottom of the respiratory tract [11,12]. Natural respiratory activities such as breathing, talking, and coughing can generate a broad range of particle sizes, from submicron aerosols to large droplets [12,13]. After being declared as a public health emergency of international concern, recommendations for protection and prevention of COVID transmission were published [14]. Among all the personal protective equipments (PPEs), face masks and respirators have been widely used as first-protection equipment and are of critical importance to prevent the spread of the aerosols and respiratory droplets especially when the social distancing measures are difficult to maintain [15–17]. As illustrated in Fig. 1, respiratory particles, which can remain in the air for some time as a result of coughing, sneezing, speaking or exhaled breath, can carry airborne pathogens and compounds and are one of the transmission routes for the infectious diseases [18–26]. Comprehensive reviews on face masks have been recently published to inform public, academia, and industry [27,28]. Karmacharya et al. [29] focused on filtration, self-sterilizing and self-cleaning capabilities of facemasks, type of facemasks, critical parameters for filtration efficiency, and existing decontamination methods. Possible use of novel antimicrobial material technologies for infection prevention clothing were discussed in depth and successfully implemented by Cano-Vicent et al. [30] and Takayama et al. [31]. Moreover, Tcharckhtchi et al. [32] presented a literature ranging from different kinds of facemasks, their application areas, advantages and drawbacks to the influence of external parameters (such as, particle size, air flow velocity), and filter characteristics (for instance, filter thickness and packing density). Tanisali et al. [33] compared the effectiveness of different face masks from cloth mask to N95 masks in aerosol dispersion in SARS-CoV-2 infection. The meta-analysis in [34] concluded that the use of face masks by public reduces the risk of transmitting respiratory infections, such as, influenza, SARS-CoV-2.

Although PPEs in occupational hygiene areas are subjected to strict testing standards and guidelines, including ISO 9237:1995 standard for determination of permeability of fabrics to air, EN 149 standard for testing and marking requirements for filtering half masks (FFP1-2-3), EN 14683:2019 (Type I-II-IIR) and ASTM F2100 (Level 1-2-3) standards describing the requirements and testing methods of medical masks, ordinary face masks and alternative options (scarfs, kerchiefs, etc.) in our daily lives do not necessarily follow these standards [35–37]. As being sold nowadays online and in the retail shops, these masks have wide-range of styles, fabrics and number of layers (also known as plies). However, their performance metrics, in terms of the particle filtration efficiencies (PFEs) and air permeability, often vary and are yet to be well rationalized and correlated with their intrinsic microstructural properties [38,39]. The first metric is important for reducing the disease transmission while the latter is essential for the breathability, i.e. wearer comfort.

Therefore, in order to correlate the mask performance and microstructure, an assessment framework was developed combining the X-ray microtomographic 3D imaging and computational fluid dynamics (CFD) methods. The investigations were limited to the prevalent off-the-shelf two layer face masks (made out of two non-woven fabric layers) and surgical masks (made out a of melt-blown fabric layer covered with two non-woven fabric layers). As shown in Fig. 2, X-ray microtomography was used to extract the geometric details of these masks at micrometer length scale and used as the solution domain for the CFD simulations. In the PFE analyses, the smoothed particle hydrodynamics (SPH) method was used to examine the particle movements through layers and focused on a spectrum of {0.1, 0.3, 0.5, 1.0, 2.0} μm particle diameters representing the aerosols. Simultaneously, finite volume method (FVM) was implemented to investigate the air permeability of these masks. The results demonstrate that the surgical masks provide PFEs over 75% for particles with a diameter over 0.1μm while two layer face masks are found to have insufficient PFEs, even for particles with a diameter over 2μm (the corresponding PFE is computed as 47.2%).

Based on the research findings, a computational design framework was also proposed for the next generation off-the-shelf masks. With this design framework, the effects of fiber diameter, orientation distribution and network density of non-woven fabric layers on the breathability and PFE were examined. In this research, breathability can be described as a degree of a fabric permitting air to pass through. The degree of breathability is disproportional to pressure drop while air passes through the facemask. Hence, the optimum/optimal design in terms of breathability can be assumed to be the one with the lowest pressure drop. The numerical results indicated that face masks with at least one melt-blown layer with randomly oriented fibers having diameter of app. 6.5μm, and higher stretching percentages in the thickness direction provided relatively high PFE with good air permeability.

2. Methods

2.1. Micro-computed tomography and mesh generation

For the microstructural analysis and volume reconstruction purposes, approximately 2mm wide strips were cut from each mask using a surgical knife. The strips were attached on to the top of carbon fibre sample holder rods using cyanoacrylate glue. Care was taken to avoid separation of the mask plies and imbibition of the glue into the imaged region of the strip.

The mounted strips were imaged with 1.15μm pixel size using an Xradia MicroXCT-400 tomograph. X-ray tube acceleration voltage and power were set to 30 kV and 4 W, respectively, for optimal contrast and resolution. A total of 1750 projection radiographs were taken with 10× optical magnification and 5 s exposure time for each radiograph. The total imaging time was approximately 7.5h per sample, including an 1.5h stabilization period at the beginning of the imaging process.

The projection images were reconstructed into a volumetric 3D image using the filtered backprojection algorithm implemented in the pi2 software[1] (version 3). Both absorption and phase reconstructions using the Paganin method [40] were made. In the reconstructed images, the fibres forming the layers of the mask are shown as bright regions on a dark background corresponding to air. Relatively high contrast-to-noise ratio allowed segmentation of the fibres from the background by applying Otsu thresholding [41] to both reconstructions. The absorption contrast image was further refined by removing all isolated foreground regions whose volume was less than 500 voxels, as these regions were

[1] Available at https://github.com/arttumiettinen/pi2.

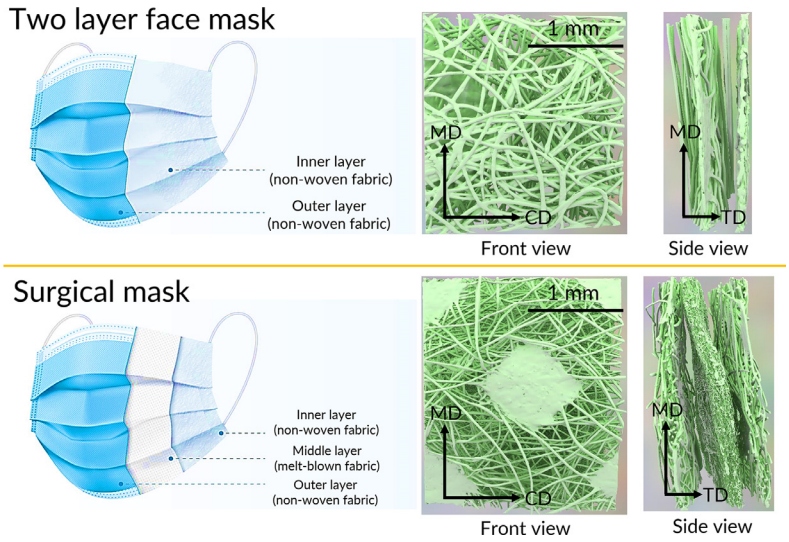

Fig. 2. Two layer face mask and surgical mask: their layer representations (left) and microstructures obtained via X-ray microtomographic 3D imaging (right). Non-woven and melt-blown fabric layers provide mechanical and electrostatic filtration, respectively. Here, CD, MD and TD refer to machine-, cross- and thickness directions for layers, respectively. Here, the solidified diamond-shaped spots represent the bond points of non-woven fabric layers as a result of hot calendering process.

likely caused by imaging noise and/or imaging artefacts, and were not part of the mask structure showing as a large connected foreground region. An example of the output of each of the processing stages is shown in Fig. 3.

In the absorption contrast image the smallest fibres are well defined, but the larger ones show significant phase-contrast artefacts. Consequently, the smallest fibres are well segmented in the absorption contrast segmentation, and the larger ones in the phase-contrast segmentation. In order to account for this while keeping the maximum resolution, the segmentations made from both reconstructions were combined using boolean OR operation to form the final binary image representing the fibre phase (see Fig. 3).

Finally, the binary images were converted to surface meshes using the iso2mesh toolbox[2] (version 1.9.0) [42,43]. The binary images were first downsampled to one half, followed by triangular isosurface extraction using the 'simplify' strategy of the `vol2surf` function. The `keepratio` parameter was set to 0.1. The final surface mesh was saved as an `.stl` file.

2.2. Computational fluid dynamics simulations

2.2.1. Particle simulations

The present computational assessment strategy mainly focuses on aerosol filtration, i.e., particles with a diameter less than 5µm, and air permeability simulations, which does not account for the variations of particle emissions [44]. The filtration was evaluated with use of SPH, a mesh-free Lagrangian particle method, i.e., particles having masses move together with the material while computing the value of physical parameters through the weighted contributions of the neighboring particles [45,46]. Because of being a mesh-free method, SPH does not suffer from large deformations and mesh distortions [47]. Therefore, it is a convenient method to treat dynamic problems such as fluid flows, spraying and ballistics in a relatively natural manner, which has been validated with the vast number of experiments and benchmark problems elaborated in the literature [48–52]. In the present study, the mass conservation was satisfied with the constant particle number and densities ρ while the conservation of momentum in terms of Navier-Stokes formulation is expressed as

$$\rho \frac{Dv}{Dt} = -\nabla p + \mu \nabla^2 v + \rho g, \tag{1}$$

where $\frac{Dv}{Dt}$ is the substantial derivative of the velocity, ∇p is the pressure gradient, g is the gravitational acceleration, $\nabla^2 v$ is the Laplacian of the velocity, μ is the dynamic viscosity. Eq. 1 was solved in the scheme of explicit central-difference time integration algorithm and time histories of the field variables for all the particles were obtained with the Abaqus/Explicit solver [53]. The relationship between the pressure p and density ρ for particles, which were assumed to possess the mechanical characteristics of water, was expressed with the linear Us-Up Hugoniot form of the Mie-Gruneisen equation of the state as [54]

$$p = \frac{\rho_0 c_s^2 \eta}{(1 - s\eta)^2}\left(1 - \frac{\Gamma_0 \eta}{2}\right) + \Gamma_0 \rho_0 E_m. \tag{2}$$

Here, E_m is the internal energy per unit mass and η is the nominal volumetric strain. The speed of sound c_s and reference density ρ_0 were taken as 1.425×10^6 mm/s and 1×10^{-9} tonne/mm^3, respectively. The material constants Γ_0 and s were assumed to be 0.28 and 1.75, respectively [55]. In addition, the Abaqus built-in surface behavior formulation was also used to (I) prevent the particle penetration to each other and the mask layer surfaces and (II) characterize the particle movements within the layers. Based on the experimental studies on friction coefficient of fabrics, Coulomb friction of 0.25 was used for non-woven fabric layers while Abaqus built-in ROUGH keyword was used for the surface friction of melt-blown fabric layers mimicking its electrostatic adsorption characteristics [56,57]. Therefore, with the provided layer surface conditions, particles colliding with fibers experience friction, which decreases their kinetic energy. If the friction cancels the momentum of the particle, the particle sticks on the fiber; thus, cannot penetrate into the other side of the mask layer.

2.2.2. Simulation of flow behaviour

The finite volume method (FVM) in STAR CCM+ was utilised to compute flow field around the investigated fibrous mediums [58]. The microstructure of these mediums is the key parameter causing resistance to flow, which is the fundamental reason for the pressure drop ΔP that maintains the pressure level at lungs and accommodates the required airflow for breathing. Together with this,

[2] Available at https://iso2mesh.sourceforge.net

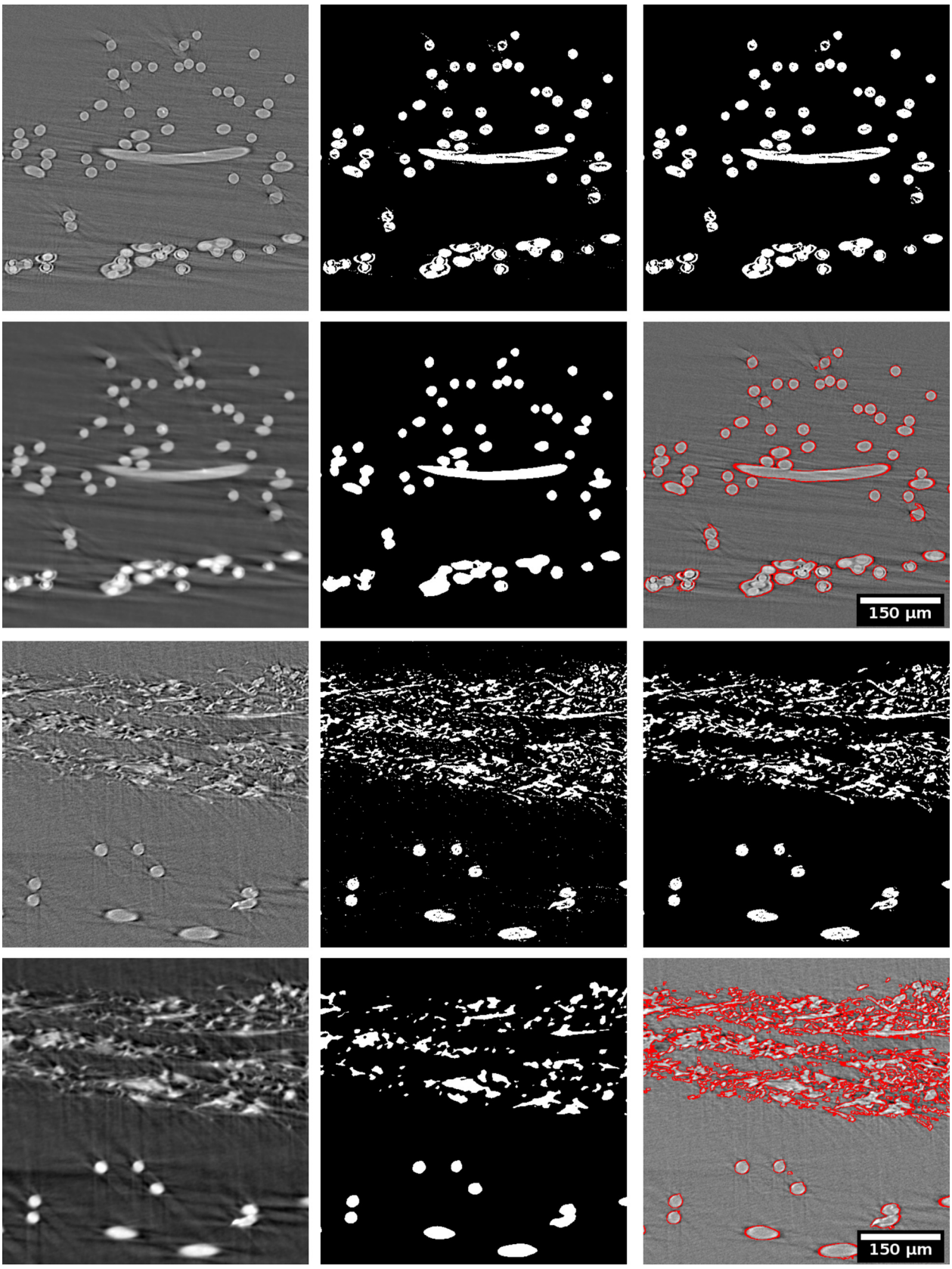

Fig. 3. Cross-sectional slices through the CT image of the two-layer mask sample (top two rows) and surgical mask sample (bottom two rows) and in various processing phases. First row from left to right: Absorption reconstruction, the same location after Otsu thresholding, and after small foreground region removal. Second row: Phase reconstruction, the same location after Otsu thresholding, and the edges of the final segmentation overlaid on the original absorption reconstruction. The third and the fourth rows follow the same format. The same scale bar applies to all the panels.

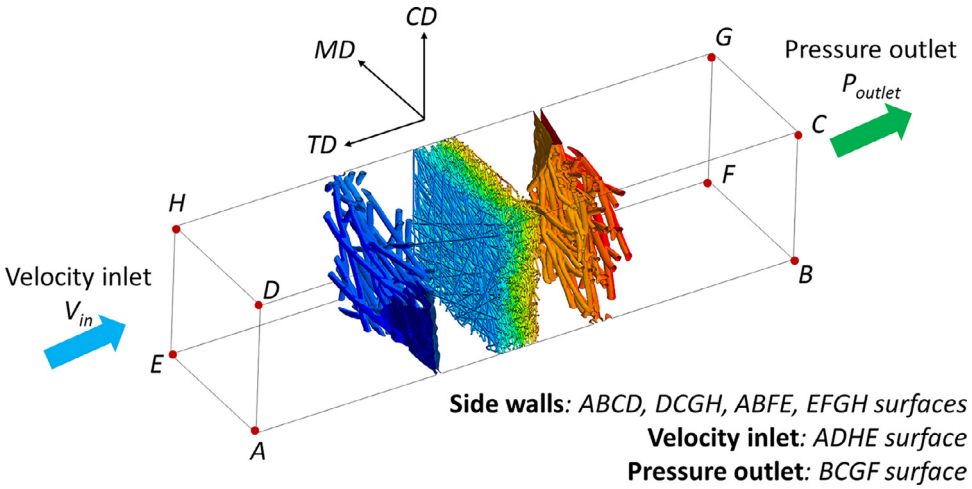

Fig. 4. Boundary conditions over flow domain: velocity inlet, pressure outlet, and side walls.

air permeability, the key performance parameter of breathability or an assessment metric the face-mask wearer comfort, is inversely proportional to ΔP. Permeability of the fibrous networks is formulated with Darcy's Law as follows

$$k = \frac{\mu \cdot t_{web} \cdot V_f}{\Delta P} \tag{3}$$

where t_{web} and V_f are the thickness of the fibrous network and face velocity of the fluid (air in our case), respectively [59]. The unknown parameter in the permeability equation is ΔP, which is predominantly influenced by the microstructure of porous medium. Analytical or empirical models for estimating the ΔP parameter are proposed in literature, such as [60,61]. Both the analytical and empirical flow models rely on the simplifications in the geometry of microstructure and flow behaviour. The actual microstructure of non-woven face masks include more complexities such as random alignments of fibres and fibre-to-fibre contacts controlling interconnected pore network. Some theoretical models in literature such as [62–65] were proposed to estimate permeability of simple fibre networks. These models express permeability in terms of only fibre volume fraction and they over-predict or under-predict actual values. They can be, however, used for verification of numerical simulations to some extent. The air flow domain in this case is a cuboid, where the front and back surfaces are defined as the velocity inlet and pressure outlet, respectively (see Fig. 4). ΔP is the difference between inlet and outlet pressures. A no slip boundary condition was implemented to the surface of the fibre surfaces, whereas a slip boundary condition was used to model shear behaviour of air flow on side walls. The base criteria for no-slip BC on the fibres is the Knudsen number K_n, defining which flow regime is valid around a fibre. When $K_n < 0.001$, a no-slip with continuum flow regime is valid around each fibre [66]. As the solution domain size for the present flow simulations are large enough, the slip condition for the side walls simply mimics and satisfies the actual BCs. For non-woven materials, there are three orthogonal directions (TD: Through-thickness Direction, CD: Cross Direction, and MD: Machine Direction). MD and CD are known as in-plane directions and TD is the direction between the inlet-outlet. There is no lateral flow (in CD and MD) in side walls and the general flow regime obeys laminar flow conditions. Because isothermal flow was considered, no heat transfer equations were solved during the simulations. The simulations for both types of face mask were repeated for three different inlet flow velocities (100 mm/s, 250 mm/s and 1000 mm/s), which are in line with the recent investigations mimicking the human breathing conditions [67–69]. The chosen atmospheric pressure conditions were valid over all the boundaries and, hence, pressure at the outlet was zero due to pressure force equilibrium. The CT-based CAD models were imported in STAR CCM+ and, the fluid domain around the fibre walls was discretized with unstructured polyhedral cells. The governing equations (continuity and momentum equations) of air flow behaviour was solved by use of a segregated fluid flow solver, where fluid pressure and velocity fields are decoupled. Convergence of the solution was monitored with residuals of momentum and mass equations in all directions.

3. Results

3.1. Particle filtration efficiency and air permeability of the face masks for community use

For the particle filtration efficiency (PFE), the total volume of 100µl particle agglomerate was expelled over approximately 1mm × 1mm mask surface area and monitored for t= 50ms, which is based on the respiratory particle aggregate formation period investigated by Wang et al. [70]. The initial particle agglomerate was formed with a script that both generates uniformly distributed pseudorandom particles and simultaneously avoids the particle penetration. Three sets of simulations were designed for each case by using the script. Following the proposed velocity ranges for the particle filtration in the literature, an inlet flow velocity of 1000mm/s (exhalation) was used [67,71]. Adapting the filtration efficiency definition in the literature [32,72], PFE was evaluated as the ratio between the number of particles heaped over the fiber surfaces and the total number of particles expelled within the investigated duration.

Average diameter of fibres in two layer non-woven medium are measured from X-ray volume data as 35µm. For the three-layer porous medium, on the other hand, the mask is composed of two calendared fabric layers (front and rear ones) and one melt-blown fabric layer (middle one) with 35µm and 6.5µm diameter fibres, respectively.

Particle filtration and air permeability performances of the investigated face masks were successfully simulated. Streamlines in the flow domains were computed with respect to flow path and projected fluid pressure over the fibres were presented in Figure 5 (a-d).. The corresponding permeability and permeability values are reported in Table 1. Comparing the tabulated air permeability values, two layer masks were deduced to be more comfortable to use rather than surgical masks. However, they have less PFEs than surgical masks, e.g., approximately 25% for submicron particles and 50% for particles over 2µm. This shows that masks comprising only

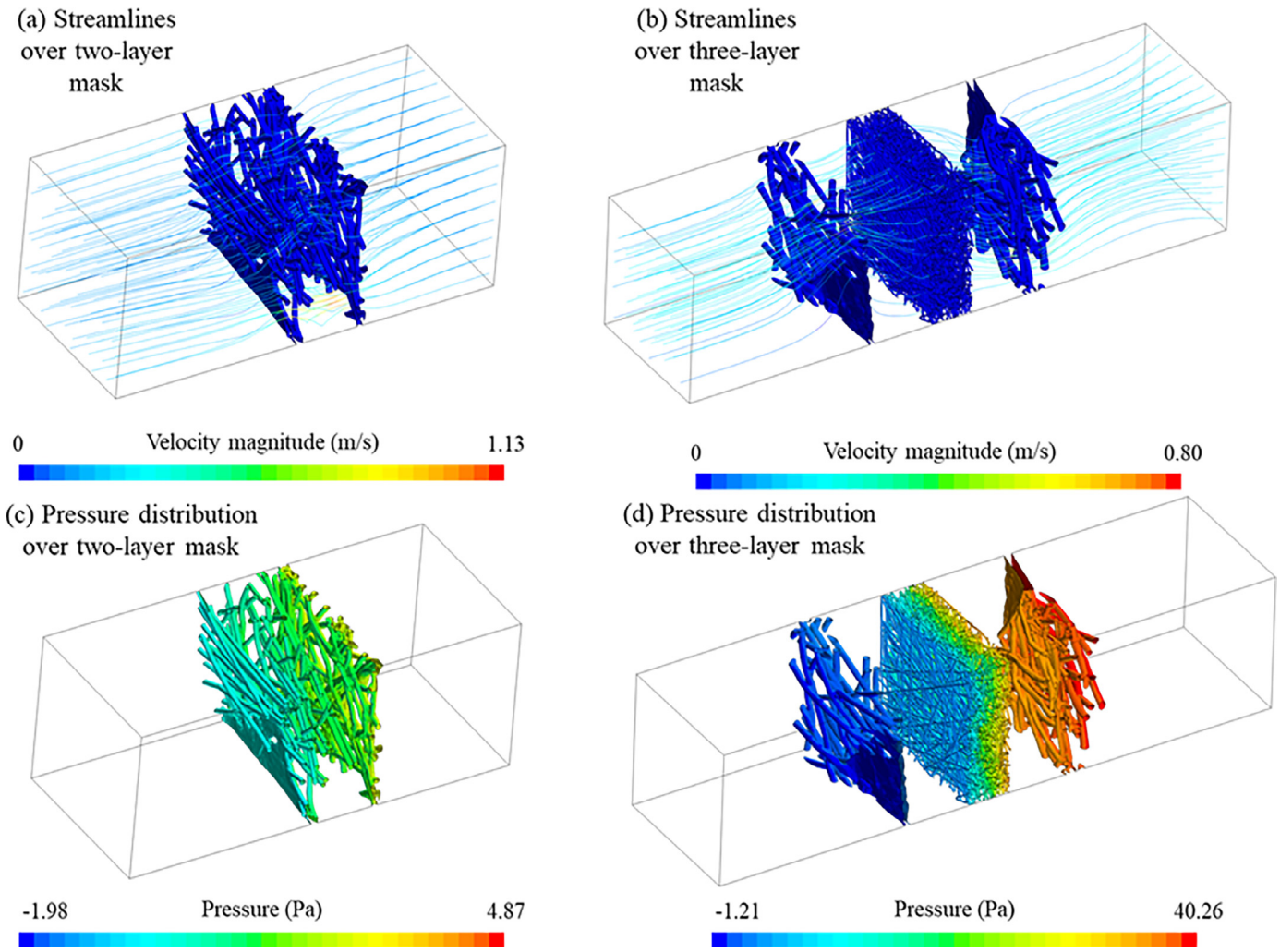

Fig. 5. Streamlines around fibres of two- and three layer face mask models (a-b) and pressure distributions over their fibres (c-d).

Table 1
Comparison of average values for air permeability and particle filtration efficiencies (PFEs) of the prevalent two- and three layer face masks for community use. $*$: The filtration efficiencies in [57] are the weighted averages for the particle size ranges less than or more than 0.3μm. $**$: The filtration efficiencies in [73] are averaged for submicron particles.

Mask type	Air permeability	Filtration by particle size (%)				
	m^2	0.1μm	0.3μm	0.5μm	1.0μm	2.0μm
Two layer mask (Present)	5.99×10^{-7}	15.8	16.8	22.7	32.4	47.2
Two layer mask [74]				20	26	<71
Two layer mask [75]			20	40		
Surgical mask (Present)	2.86×10^{-8}	77.0	77.2	77.8	81.7	90.2
Surgical mask* [57]		76				99.6
Surgical mask** [73]			71.5			

two non-woven layers provide significantly less protection against spreading the disease.

The face velocity of air flow through the filter medium was between 100 mm/s and 1000 mm/s, which is relatively high for particle trapping due to diffusion. We, therefore, assumed the leading particle deposition mechanisms are impaction and interception. This implies particles are mainly captured by the fibre surfaces encountering aerosols.

3.2. Design recommendations and future directions for next generation face masks

The simulated results over the prevalent face masks indicated that there is a room for development in consideration to both PFE and permeability. For this reason, a computational design framework for improving mask protection and wearer comfort was proposed. First, mock-up models of two layer face masks emulating actual microstructure extracted from CT images were generated with finite-element simulations, where 3D fibers were stacked on the top of each other in the through-thickness direction (TD). To have a realistic microstructure, constituent fibres were in contact and possible penetrations were minimised with contact algorithms [76–79]. Using in-house algorithms written in Python, the generated models in FE environment were converted into CAD models in Autodesk Fusion to be imported in Star CCM+ for CFD simulations.

The aforementioned particle simulations for both types of face masks demonstrated the significance of presence of melt-blown

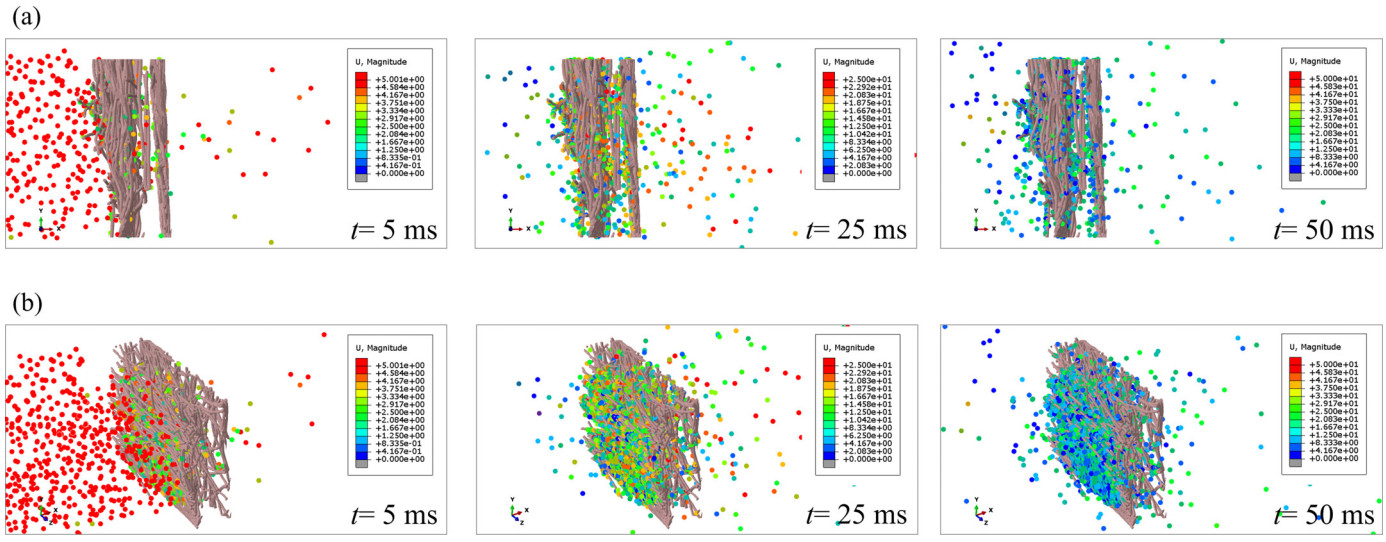

Fig. 6. Particle movement simulations through reconstructed two layer mask at different time intervals of $t = 5ms$, $t = 25ms$, $t = 50ms$: (a) side view, (b) isometric view. Here, U refers to the displacement magnitude in millimeters.

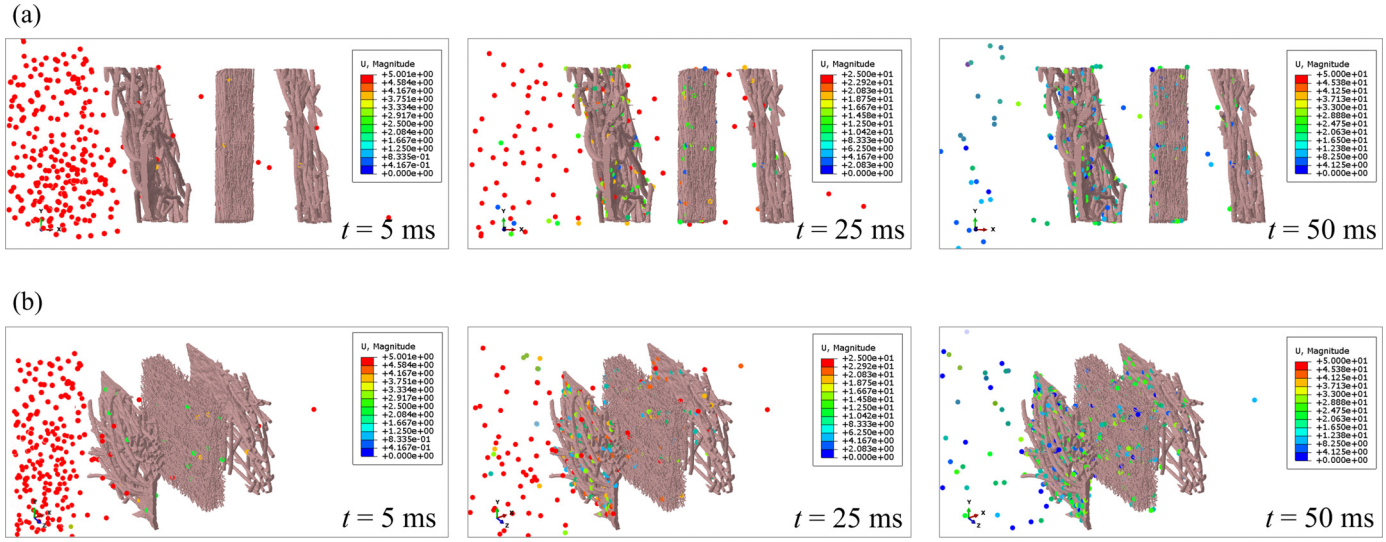

Fig. 7. Particle movement simulations through reconstructed three layer surgical mask at time intervals of $t = 5$ms, $t = 25$ms, $t = 50$ms: (a) side view, (b) isometric view. Here, U refers to the displacement magnitude in millimeters.

layer on the PFE. The amount of material in each layer of two- and three layer face masks was measured to be the same ($20g/m^2$). Two non-woven layers ($40g/m^2$ in total) with 35µm fibres in the two layer face mask only filtered 20–25% of aerosols with a particle size of 0.3µm whereas a single melt-blown layer with 6.5µm fibres in a three layer face mask achieved to filter over 80% of them. In comparison with the prevalent off-the-shelf mask investigations, 15%-20% more PFE was achieved with the new design configurations.

Four unique geometries for each non-woven face mask were generated to investigate the effect of microstructure on filtration and permeability performances. Henceforth, orientation distribution of fibers, fibre diameter, and fiber network density were examined on the performance parameters. Fig. 8(a)–(d) presents the input parameters for each design case. Design 1 forms the base model for two layer face masks and the constituent fibres are randomly distributed using an uniform distribution function (*f1*) in the MD-CD plane. This random distribution was implemented into both layers of the two layer mask microstructure and the resultant fibrous network of the Design 1 is shown in Fig. 8(b). Different than the distribution *f1*, a normal distribution *f2* (see Fig. 8(c)) enabling preferentially aligned fibers in MD are also tested for both type of face masks.

3.2.1. Fiber diameter, orientation distribution and network density

Based on the numerical findings, need for the structural development was deduced to be inevitable for the commonly used face masks. Such developments can be carried out through testing different microstructural parameters, such as, the fiber diameter, orientation distribution, and network density, for which a good balance should be determined. For this reason, various design cases were developed and simulated for non-woven layers as represented in Figs. 8 and 9. Designs 1 and 2 was used to quantify the contribution of the orientation distribution of fibers to the permeability and filtration capacity of two layer face masks. For non-woven face masks, the permeability measurements through thickness direction (TD) and transverse planes (TD-CD and TD-MD) are of main interests. The previous works such as [80,81] focused on transverse (i.e. through-thickness direction (TD)) air permeability of fibrous networks. They demonstrated that the transverse per-

(a) Parametric investigation of 2-layer facemask

Case ID	Design 1	Design 2	Design 3	Design 4
Orientation distribution of fibers $p(\alpha)$	*f1*	*f2*	*f1*	*f1*
Fiber diameter (μm)	35	35	25	35
Deformation in TD*	0%	0%	0%	-50%

*TD: Through-thickness Direction

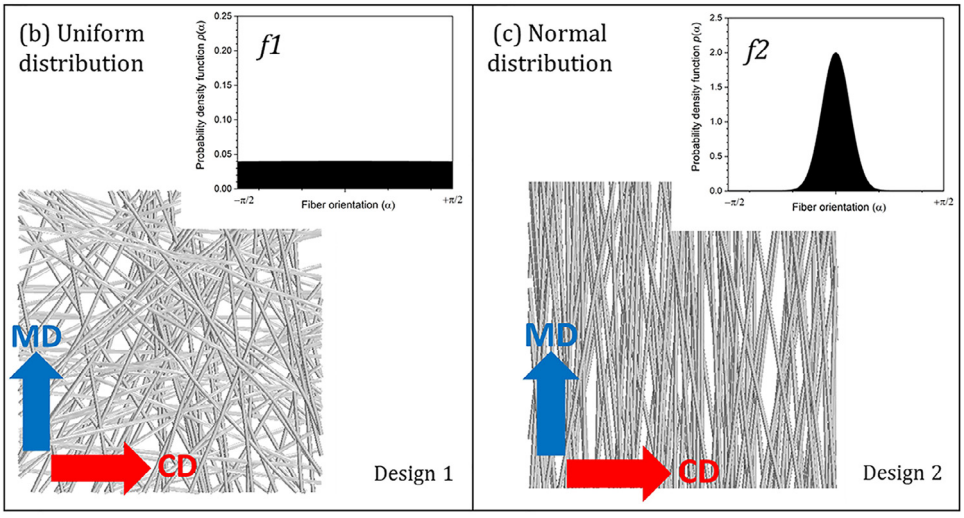

(d) Parametric investigation of 3-layer facemask

Case ID	Design 5	Design 6	Design 7	Design 8
Orientation distribution of fibers $p(\alpha)$	*f1*	*f1*	*f1*	*f2*
Fiber diameter (μm)	6.5	6.5	6.5	6.5
Deformation in TD*	0%	-50%	+50%	0%

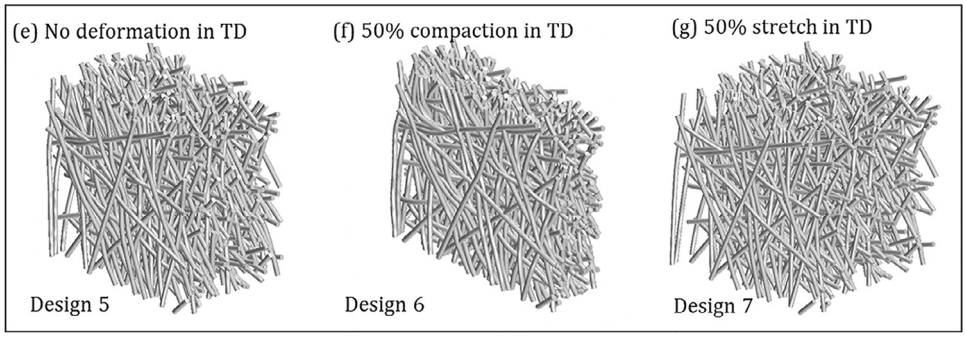

Fig. 8. (a) Parameters used for two layer mask designs; (b) representation of probability density function for random fiber network; (c) representation of probability density function for aligned fiber network; (d) parameters used for three layer mask designs; (e)-(f)-(g) three layer mask designs under 0%, 50% compaction, 50% stretch in through-thickness direction(TD), respectively.

meability is independent of in-plane fiber orientations, whereas the variations in fiber orientations in transverse planes increases the transverse permeability by opening voids allowing the fluid passing through. In addition this, Zobel et al. [82] simulated the permeability of thermally-calendered non-wovens and, afterwards, claimed that the TD permeability is independent of orientation of fibers. A 2D computational model capturing statistical randomness of fibres of the N95 facemask was suggested to predict the filtration efficiency of individual layers [83]. Our parametric models mimicking the microstructures of off-the-shelf two layer face masks and three layer surgical masks have highly aligned fibers in transverse planes, meaning fibers are parallel to MD-CD plane and perpendicular to incoming air flow. Thus, the orientations of fibers in Designs 1 and 2 were only varied in the MD-CD plane as seen in Fig. 8(a)-(b). As depicted in Fig. 9(a) for two layer face mask designs, preferentially oriented fibers decreased the PFE as

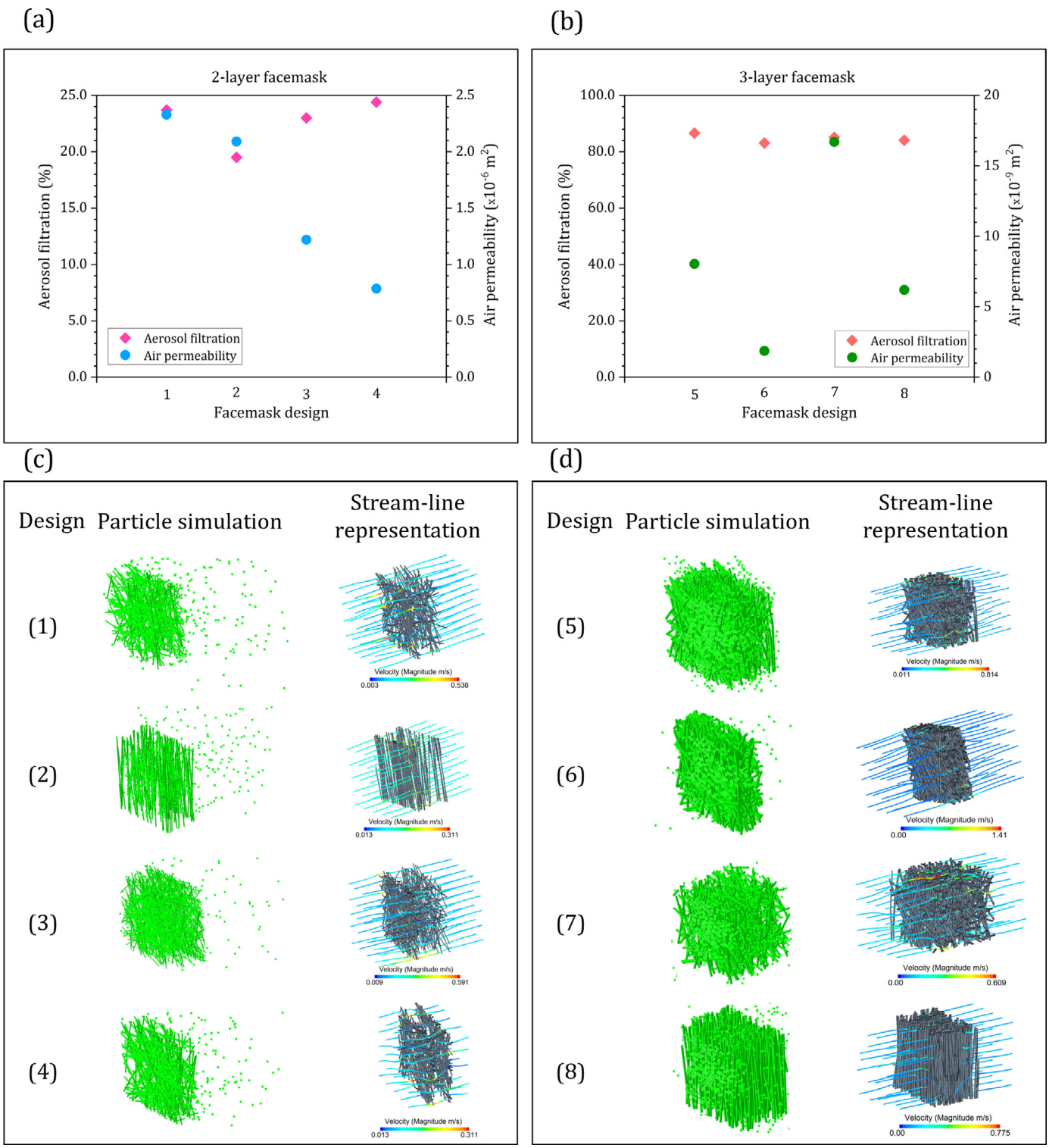

Fig. 9. Parametric analysis of particle filtration and air permeability of face masks: aerosol filtration and air permeability predictions for different two layer (a) and three layer (b) face mask designs, particle simulations and stream-line representations of two layer (c) and three layer (d) face mask designs.

well as the air permeability, by 10% and 18percent, respectively. For our two layer face mask, variations in orientation distributions of fibers in MD-CD plane, which is orthogonal to flow direction, is one of the key parameters to be strictly retained.

The common theoretical models mentioned previously, such as the ones in [62,63,65], express the permeability in terms of fibre volume fraction and diameter. The permeability is directly proportional to the square of fiber diameter. To test this argument, the diameter of fibers in Design 3 was reduced from 35µm to 25µm. Simultaneously, the PFE of the design was also assessed. The investigations resulted in a microstructure of face mask with 48% less permeability in comparison to our base model (Design 1), which is 5% away from the theoretical predictions. While reducing the fiber diameters, fibre volume fraction was retained along with the size of fibrous network model. This change, approximately, doubled the number of fibers in the model. For the tested fiber diameters, PFE

was not significantly changed. This behaviour is attributed to that the pore size of the new geometry is not sufficiently small to filter the particles. In Design 4, however, the aim was to shrink the pores in both face mask layers for potential improvement in filtration. A minor positive change in the PFE was recorded, though a significant decrease in the air permeability was obtained as a trade-off. Fig. 9 (c) demonstrates particle simulations and stream-line representations of Designs 1–4.

As for the three layer face masks, the core layer is manufactured with a melt-blown process. Despite having a similar basis weight as the front and back layers, it facilitates a fibrous network with comparatively a higher filtration efficiency. Our numerical simulations demonstrated that the major proportion of aerosol particle entrapment occurs in this layer. In the parametric studies of three layer face mask, therefore, only the core layer was modelled for permeability and filtration simulations. The design parameters of parametric designs are demonstrated in Figure 8(d). In Designs 5–7, the thickness of the core layer in TD was varied by 50% such that filtration and permeability performances are manipulated. The resultant CAD models of these fibrous networks at original, compression, and stretch states are demonstrated in Fig. 8(e)-(g). Fig. 9 (b) show the plot of aerosol filtration and air permeability predictions for Designs 5–7. Meanwhile, Fig. 9(d) demonstrates particle simulations and their stream-line representations. Apparently, from the Table 1, three layer face mask reached up to 80% filtration efficiency against the particles with 1.0µm size and, however, relatively lower air permeability in comparison with the one for two layer face mask. 6.5µm fibres were distributed by using a fully-random orientation distribution in the finite-element (FE) model and the microstructural geometry of Design 5 was produced. The same FE model was compressed by 50% to produce Design 6 and stretched by 50% to generate Design 7. The facemask layers were stretched in the thickness direction (TD), and the base model was assumed to have 0% stretch or compression. The deformed FE geometries were converted into CAD models using in-house Python scripts for flow simulations. Numerical simulations of these models suggest that the filtration efficiency of a fibrous network is independent of fiber network density (as a result of network compaction or stretching). The air permeability, however, can be fine tuned via compaction or stretching processes. In a recent work, Ando et al. [84] simulated flow-induced deformation of a fibrous media and its effect on filtration performance with a 3D fluid-structure interaction algorithm. The geometry of nonwoven media with high fiber densities (above 17%) is affected less by air flow mimicking coughing and the change in air permeability is ignorable. The implementation of 50% stretch into the melt-blown layer improved the air permeability with no significant trade-off in aerosol particle filtration. Oppositely, the two non-woven layer face mask does not need such stretch due to high existing permeability. The results obtained from Design 8 demonstrates that a fibrous medium with smaller fiber diameter, which is 6.5µm in our current case, is insensitive to orientation distribution of fibers. For instance, air permeability decreased by 25%, which is not desirable for face mask users. A face mask made from at least one melt-blown layer with small fiber diameter (as studied in current case), uniform orientation distribution *f1* of fibers, and lower fiber volume fraction can be recommended for face mask manufacturers.

4. Discussion

To the best of the authors' knowledge, the present study is one of the first microscale assessment frameworks for commonly used face masks in public, which combines both X-ray microtomographic 3D imaging and CFD simulations. Despite the invaluable macroscale face mask investigations on the transmission of respiratory infectious diseases in the literature [32,57,85], the numerical frameworks focusing on their microscale characterization and performance are almost non-existing with very few exceptions in the literature [84]. This is mainly due to the labour-intensive volume reconstruction process and ever-increasing computational costs with the solution domain. Based on these facts, the framework focused on reconstructed and generated domains within micron-to-millimeter scale range. The investigations were then conducted to understand the effects of microstructural characteristics of face mask layers, which were taken as fibre diameter, fibre orientation distribution and network density, on the filtration efficiency and permeability of two layer face masks and three layer surgical masks. Such microstructural analyses play a critical role not only to understand the performance of the prevalent off-the-shelf face masks but also to improve the face mask layer designs.

In line with the recent studies on transmitted particle sizes [83,86,87], the particle diameter range of {0.1, 0.3, 0.5, 1.0, 2.0} µm was investigated. The present numerical model with the reconstructed face mask layers did not take the particle emission and flow speed variations into account because of the scale and duration of interest, following the previous studies in the literature [44]. In addition, the airflow direction was assumed to be orthogonal to the thickness direction (TD), through which the particles properly meet the face mask layers. Under these assumptions and limitations, the model provides a microscopic insight with time intervals of $t = 50ms$ that agrees well with the recent particle image velocimetry experiments [70]. The results were also observed to be in line with the recent experimental results [87,88], showing the trade-off between the PFE and breathability in terms of air permeability. Especially, for the intermediate sizes of 0.1µm-0.3µm, the particles were obtained to be hardly captured by face masks with two non-woven layers as seen in Fig. 6, which demonstrates their insufficiency. On the other hand, surgical masks composed of two non-woven and one melt-blown layers as reconstructed in Fig. 7 were deduced to produce sufficient PFE for the particle sizes under investigations. This outcome also revealed the significance of presence of melt-blown layer, around which the most droplets are to be trapped as the droplet sizes are larger than the fibre spacing. It is also likely that the melt-blown layer work as a barrier preventing droplets to evaporate and transform into smaller particles [38].

The results obtained from the prevalent mask types were used as foundation for prospective face mask designs, through which different fiber diameter, orientation distribution, and network density configurations were examined. Based on the simulation results for these configurations, the fibre diameter was deduced to be the major factor in designing and controlling the fineness and filtration capacity of the face mask layers while the number of nonwoven layers were found out to be a less decisive parameter. These findings were found out to be inline with the investigations in the literature [89–92]. Having fibres with small diameters has a trade-off in the breathability performance of face masks, meaning lower permeability, which can be overcome by reducing the compaction ratio (fiber network density) in TD. The investigated design configurations for new generation face masks were based on circular cross-sectional fibres mimicking the ones reconstructed from the X-ray microtomography of the readily available face masks. However, several investigations, such as in [93–95], claimed that the fibres with triangular, quatrefoil, trilobal and elliptical cross-sections have higher filtration efficiency than those with circular cross-sections. Although this behaviour could be attributed to the larger specific surface area and can facilitate prospective numerical studies, production and economical feasibility of such fibers should be thoroughly investigated. Nevertheless, in order to have a face mask with high filtration efficiency and comfort in terms of breathability, the results demonstrated that a face mask should have at least one nonwoven layer with fine (small) fibres and

low compaction. Developments in non-circular fiber manufacturing processes and surface treatments would definitely be affirmative in the filtration efficiency and breathability.

5. Conclusions

The present study provides a novel and thorough assessment of the commonly used face masks in consideration to their microstructures, PFEs and air permeabilities by using X-ray microtomography and CFD simulations. A design space with the parameters defining the quality of the mask, i.e. fiber diameter, fiber network density and orientation distribution, was suggested, which aims at better protection and breathability. Hence, the introduced study and framework can be applied to design new face masks with computerized methods, which aims at minimizing the research and development efforts and costs. Although the simulations were idealized and limited based on various assumptions, the presented results can simply contribute to reducing the transmission of respiratory infectious diseases for the prospective waves of pandemic and provide better comfort for the wearer with prolonged face mask use.

Statement of ethical approval

There was no participation of human or animal subjects during the investigations; therefore, the present study did not require any statement of ethical approval.

Declaration of Competing Interest

The authors declare they have no known competing financial interests of personal relationships that could have appeared to influence the work reported in this paper.

Acknowledgements

A.K., H.Y. and R.J. also acknowledges the funding through Academy of Finland BESIMAL (Decision No. 334197) and Aalto University, Department of Communications and Networking. This work has also received funding in part from the EPSRC UK (grant number EP/R012091/1). A.K. would also like to thank Mr. Volkan Kaplan for the fruitful discussions in the early concept generation.

References

[1] X.S. Zhang, C. Duchaine, SARS-CoV-2 and health care worker protection in low-risk settings: a review of modes of transmission and a novel airborne model involving inhalable particles, Clin. Microbiol. Rev. (2020), doi:10.1128/CMR.00184-20.
[2] C. Wang, P.W. Horby, F.G. Hayden, G.F. Gao, A novel coronavirus outbreak of global health concern, Lancet (2020), doi:10.1016/S0140-6736(20)30185-9.
[3] E. Callaway, D. Cyranoski, China coronavirus: six questions scientists are asking, Nature (2020), doi:10.1038/d41586-020-00166-6.
[4] S.-y. Pan, M. Ding, J. Huang, Y. Cai, Y.-z. Huang, Airway resistance variation correlates with prognosis of critically ill COVID-19 patients: a computational fluid dynamics study, Comput. Methods Programs Biomed. 208 (2021) 106257.
[5] Y. Wang, B. Li, R. Gouripeddi, J.C. Facelli, Human activity pattern implications for modeling SARS-COV-2 transmission, Comput. Methods Programs Biomed. 199 (2021) 105896.
[6] S. Singh, R. Aburashed, G. Natale, Cfd based analysis of 3d printed nasopharyngeal swabs for COVID-19 diagnostics, Comput. Methods Programs Biomed. (2022) 106977.
[7] World Health Organization (WHO), Coronavirus Disease 2019 (COVID-19): Situation Report 73, Technical Report, Who, 2020.
[8] S. Tang, Y. Mao, R.M. Jones, Q. Tan, J.S. Ji, N. Li, J. Shen, Y. Lv, L. Pan, P. Ding, X. Wang, Y. Wang, C.R. MacIntyre, X. Shi, Aerosol transmission of SARS-COV-2? Evidence, prevention and control, Environ. Int. (2020), doi:10.1016/j.envint.2020.106039.
[9] S.S. Abdool Karim, T. de Oliveira, New SARS-COV-2 variants clinical, public health, and vaccine implications, N. Engl. J. Med. (2021).
[10] S. Asadi, A.S. Wexler, C.D. Cappa, S. Barreda, N.M. Bouvier, W.D. Ristenpart, Aerosol emission and superemission during human speech increase with voice loudness, Sci. Rep. (2019), doi:10.1038/s41598-019-38808-z.
[11] J.Y. Chan, E.W. Wong, W. Lam, Practical aspects of otolaryngologic clinical services during the 2019 Novel Coronavirus Epidemic:, 2020, An Experience in Hong Kong. 10.1001/jamaoto.2020.0488
[12] L. Bourouiba, Turbulent gas clouds and respiratory pathogen emissions:, 2020, Potential Implications for Reducing Transmission of COVID-19. 10.1001/jama.2020.4756
[13] M.I. Guzman, An overview of the effect of bioaerosol size in coronavirus disease 2019 transmission, Int. J. Health Plann. Manage. (2020).
[14] World Health Organization (WHO), Infection Prevention and Control During Health Care when COVID-19 is Suspected, Technical Report, Who, 2020.
[15] A.V. Mueller, M.J. Eden, J.M. Oakes, C. Bellini, L.A. Fernandez, Quantitative method for comparative assessment of particle removal efficiency of fabric masks as alternatives to standard surgical masks for PPE, Matter (2020), doi:10.1016/j.matt.2020.07.006.
[16] J.D.M. Douglas, N. McLean, C. Horsley, G. Higgins, C.M. Douglas, E. Robertson, COVID-19: smoke testing of surgical mask and respirators, Occup. Med. (2020), doi:10.1093/occmed/kqaa167.
[17] K.-F. Ho, L.-Y. Lin, S.-P. Weng, K.-J. Chuang, Medical mask versus cotton mask for preventing respiratory droplet transmission in micro environments, Sci. Total Environ. 735 (2020) 139510.
[18] K.V. Holmes, SARS-associated Coronavirus, N. Engl. J. Med. (2003), doi:10.1056/nejmp030078.
[19] W.G. Lindsley, J.S. Reynolds, J.V. Szalajda, J.D. Noti, D.H. Beezhold, A cough aerosol simulator for the study of disease transmission by human cough-generated aerosols, Aerosol Sci. Technol. (2013), doi:10.1080/02786826.2013.803019.
[20] B. Wang, A. Zhang, J.L. Sun, H. Liu, J. Hu, L.X. Xu, Study of SARS transmission via liquid droplets in air, J Biomech Eng (2005), doi:10.1115/1.1835350.
[21] Y. Zheng, H. Chen, M. Yao, X. Li, Bacterial pathogens were detected from human exhaled breath using a novel protocol, J. Aerosol Sci. 117 (2018) 224–234.
[22] Y.R. Guo, Q.D. Cao, Z.S. Hong, Y.Y. Tan, S.D. Chen, H.J. Jin, K.S. Tan, D.Y. Wang, Y. Yan, The origin, transmission and clinical therapies on Coronavirus Disease 2019 (COVID-19) outbreak- an update on the status, Mil. Med. Res. (2020), doi:10.1186/s40779-020-00240-0.
[23] B. Bostanci Ceran, A. Karakoç, E. Taciroğlu, Airborne pathogen projection during ophthalmic examination, Graefe's Arch. Clin. Exp. Ophthalmol. (2020), doi:10.1007/s00417-020-04815-4.
[24] L. Morawska, D.K. Milton, It is time to address airborne transmission of Coronavirus Disease 2019 (COVID-19), Clin. Infect. Dis. (2020), doi:10.1093/cid/ciaa939.
[25] V. Vuorinen, M. Aarnio, M. Alava, V. Alopaeus, N. Atanasova, M. Auvinen, N. Balasubramanian, H. Bordbar, P. Erästö, R. Grande, N. Hayward, A. Hellsten, S. Hostikka, J. Hokkanen, O. Kaario, A. Karvinen, I. Kivistö, M. Korhonen, R. Kosonen, J. Kuusela, S. Lestinen, E. Laurila, H.J. Nieminen, P. Peltonen, J. Pokki, A. Puisto, P. Råback, H. Salmenjoki, T. Sironen, M. Österberg, Modelling aerosol transport and virus exposure with numerical simulations in relation to SARS-COV-2 transmission by inhalation indoors, Saf. Sci. (2020), doi:10.1016/j.ssci.2020.104866.
[26] S.K. Bhardwaj, N. Bhardwaj, V. Kumar, D. Bhatt, A. Azzouz, J. Bhaumik, K.-H. Kim, A. Deep, Recent progress in nanomaterial-based sensing of airborne viral and bacterial pathogens, Environ. Int. 146 (2021) 106183, doi:10.1016/j.envint.2020.106183.
[27] A. Tuñón-Molina, K. Takayama, E.M. Redwan, V.N. Uversky, J. Andrés, Á. Serrano-Aroca, Protective face masks: current status and future trends, ACS Appl. Mater. Interfaces 13 (48) (2021) 56725–56751.
[28] J. Howard, A. Huang, Z. Li, Z. Tufekci, V. Zdimal, H.-M. van der Westhuizen, A. von Delft, A. Price, L. Fridman, L.-H. Tang, et al., An evidence review of face masks against COVID-19, Proc. Natl. Acad. Sci. 118 (4) (2021). e2014564118
[29] M. Karmacharya, S. Kumar, O. Gulenko, Y.-K. Cho, Advances in facemasks during the COVID-19 pandemic era, ACS Appl. Bio Mater. 4 (5) (2021) 3891–3908, doi:10.1021/acsabm.0c01329.
[30] A. Cano-Vicent, A. Tuñón-Molina, M. Martí, Y. Muramoto, T. Noda, K. Takayama, Á. Serrano-Aroca, Antiviral face mask functionalized with solidified hand soap: low-cost infection prevention clothing against enveloped viruses such as SARS-COV-2, ACS Omega 6 (36) (2021) 23495–23503.
[31] K. Takayama, A. Tuñón-Molina, A. Cano-Vicent, Y. Muramoto, T. Noda, J.L. Aparicio-Collado, R. Sabater i Serra, M. Martí, Á. Serrano-Aroca, Non-woven infection prevention fabrics coated with biobased cranberry extracts inactivate enveloped viruses such as SARS-COV-2 and multidrug-resistant bacteria, Int. J. Mol. Sci. 22 (23) (2021) 12719.
[32] A. Tcharkhtchi, N. Abbasnezhad, M. Zarbini Seydani, N. Zirak, S. Farzaneh, M. Shirinbayan, An overview of filtration efficiency through the masks: mechanisms of the aerosols penetration, Bioactive Mater. 6 (1) (2021) 106–122, doi:10.1016/j.bioactmat.2020.08.002.
[33] G. Tanisali, A. Sozak, A.S. Bulut, T.Z. Sander, O. Dogan, C. Dag, M. Gonen, F. Can, H. Demirci, O. Ergonul, Effectiveness of different types of mask in aerosol dispersion in SARS-COV-2 infection, Int. J. Infect. Dis. 109 (2021) 310–314.
[34] K. Chaabna, S. Doraiswamy, R. Mamtani, S. Cheema, Facemask use in community settings to prevent respiratory infection transmission: a rapid review and meta-analysis, Int. J. Infect. Dis. 104 (2021) 198–206, doi:10.1016/j.ijid.2020.09.1434.
[35] International Organization for Standardization, ISO 9237:1995 Textiles Determination of the permeability of fabrics to air, 2017, air.
[36] European Committee for Standardization, EN 14683:2019 Medical face masks, 2019, requirements and test methods.

[37] ASTM F2100, Standard specification for performance of materials used in, 2019, medical face masks.
[38] W. Du, F. Iacoviello, T. Fernandez, R. Loureiro, D.J. Brett, P.R. Shearing, Microstructure analysis and image-based modelling of face masks for COVID-19 virus protection, Communications Materials 2 (1) (2021) 1–10.
[39] H.R. Lee, L. Liao, W. Xiao, A. Vailionis, A.J. Ricco, R. White, Y. Nishi, W. Chiu, S. Chu, Y. Cui, Three-dimensional analysis of particle distribution on filter layers inside n95 respirators by deep learning, Nano Lett. 21 (1) (2020) 651–657.
[40] P. D, M. SC, G. TE, M. PR, W. SW, Simultaneous phase and amplitude extraction from a single defocused image of a homogeneous object, J. Microsc. 206 (2002) 33–40.
[41] O. N, Threshold selection method from gray-level histograms, IEEE Trans. Syst. ManCubernetics (1979).
[42] Q. Fang, D. Boas, Tetrahedral mesh generation from volumetric binary and gray-scale images, in: Proceedings of IEEE International Symposium on Biomedical Imaging, 2009, pp. 1142–1145.
[43] A.P. Tran, S. Yan, Q. Fang, Improving model-based FNIRS analysis using mesh-based anatomical and light-transport models, Neurophotonics 7 (1) (2020) 015008.
[44] H. Li, F.Y. Leong, G. Xu, C.W. Kang, K.H. Lim, B.H. Tan, C.M. Loo, Airborne dispersion of droplets during coughing: a physical model of viral transmission, Sci. Rep. 11 (1) (2021) 1–10.
[45] J.J. Monaghan, An introduction to SPH, Comput. Phys. Commun. (1988), doi:10.1016/0010-4655(88)90026-4.
[46] J.J. Monaghan, Smoothed particle hydrodynamics, Annu. Rev. Astron. Astrophys. (1992), doi:10.1146/annurev.aa.30.090192.002551.
[47] J. Xie, D. Nélias, H.W.L. Berre, K. Ogawa, Y. Ichikawa, Simulation of the cold spray particle deposition process, J. Tribol. (2015), doi:10.1115/1.4030257.
[48] M. Müller, D. Charypar, M. Gross, Particle-based fluid simulation for interactive applications, in: Proceedings of the 2003 ACM SIGGRAPH/Eurographics Symposium on Computer Animation, SCA 2003, 2003.
[49] M. Kelager, Lagrangian Fluid Dynamics Using Smoothed Particle Hydrodynamics, University of Copenhagen: Department of Computer Science, 2006.
[50] A. Colagrossi, M. Landrini, Numerical simulation of interfacial flows by smoothed particle hydrodynamics, J. Comput. Phys. (2003), doi:10.1016/S0021-9991(03)00324-3.
[51] H. Wan, R. Li, X. Pu, H. Zhang, J. Feng, Numerical simulation for the air entrainment of aerated flow with an improved multiphase SPH model, Int. J. Comput. Fluid Dyn. (2017), doi:10.1080/10618562.2017.1420175.
[52] A. Trimulyono, H. Hashimoto, Experimental validation of smoothed particle hydrodynamics on generation and propagation of waterwaves, J. Mar. Sci. Eng. (2019), doi:10.3390/jmse7010017.
[53] D.S. Simulia, Abaqus 6.14, Abaqus 6.14 Analysis User's Guide(2014).
[54] W. Yang, T. Chen, H. Wang, R. He, Simulation of medical goggles to stop airborne transmission of viruses: computational fluid dynamics in ergonomics, Ergonomics (just-accepted) (2022) 1–19.
[55] A. Constantinescu, A.E.M. Alaoui, A. Nême, N. Jacques, P. Rigo, Numerical and experimental studies of simple geometries in slamming, Int. J. Offshore Polar Eng. (2011).
[56] M. Lima, R. Vasconcelos, M.J. Abreu, M.E. Silva, Comparative study of friction coefficient in nonwovens usin frictorq, fabric friction tester, in: Proceedings of the 6th AUTEX 2006 Conference, 2006, pp. 1–9.
[57] A. Konda, A. Prakash, G.A. Moss, M. Schmoldt, G.D. Grant, S. Guha, Aerosol filtration efficiency of common fabrics used in respiratory cloth masks, ACS Nano 14 (5) (2020) 6339–6347.
[58] S.-C. Simcenter, Software package, Version 15(2020) 007–R8.
[59] C. McPhee, J. Reed, I. Zubizarreta, Core Analysis: a Best Practice Guide, Elsevier, 2015.
[60] C.N. Davies, Air filtration [by] C. N. Davies, Academic Press London, New York, 1973.
[61] J. Happel, Viscous flow relative to arrays of cylinders, AIChE J. 5 (2) (1959) 174–177, doi:10.1002/aic.690050211.
[62] M.M. Tomadakis, T.J. Robertson, Viscous permeability of random fiber structures: comparison of electrical and diffusional estimates with experimental and analytical results, J. Compos. Mater. 39 (2) (2005) 163–188, doi:10.1177/0021998305046438.
[63] A. Tamayol, M. Bahrami, Transverse permeability of fibrous porous media, Phys. Rev. E 83 (2011) 1–9.
[64] G.W. Jackson, D.F. James, The permeability of fibrous porous media, Can. J. Chem. Eng. 64 (3) (1986) 364–374.
[65] L. Spielman, S.L. Goren, Model for predicting pressure drop and filtration efficiency in fibrous media, Environ. Sci. Technol. 2 (4) (1968) 279–287, doi:10.1021/es60016a003.
[66] H. Rostamzadeh, M. Salimi, M. Taeibi-Rahni, Permeability correlation with porosity and Knudsen number for rarefied gas flow in Sierpinski carpets, J. Nat. Gas Sci. Eng. 56 (2018) 549–567, doi:10.1016/j.jngse.2018.06.037.
[67] M. Hossain, N.H. Faisal, Modeling aerosol cloud aerodynamics during human coughing, talking, and breathing actions, AIP Adv. 11 (4) (2021) 045111.
[68] C. Pei, Q. Ou, S.C. Kim, S.-C. Chen, D.Y. Pui, et al., Alternative face masks made of common materials for general public: fractional filtration efficiency and breathability perspective, Aerosol Air Qual. Res. 20 (12) (2020) 2581–2591.
[69] D. Wang, Y. You, X. Zhou, Z. Zong, H. Huang, H. Zhang, X. Yong, Y. Cheng, L. Yang, Q. Guo, et al., Selection of homemade mask materials for preventing transmission of COVID-19: a laboratory study, PLoS One 15 (10) (2020) e0240285.
[70] H. Wang, Z. Li, X. Zhang, L. Zhu, Y. Liu, S. Wang, The motion of respiratory droplets produced by coughing, Phys. Fluids 32 (12) (2020) 125102.
[71] J.W. Tang, A.D. Nicolle, C.A. Klettner, J. Pantelic, L. Wang, A.B. Suhaimi, A.Y. Tan, G.W. Ong, R. Su, C. Sekhar, et al., Airflow dynamics of human jets: sneezing and breathing-potential sources of infectious aerosols, PLoS One 8 (4) (2013) e59970.
[72] L.H. Kwong, R. Wilson, S. Kumar, Y.S. Crider, Y. Reyes Sanchez, D. Rempel, A. Pillarisetti, Review of the breathability and filtration efficiency of common household materials for face masks, ACS Nano 15 (4) (2021) 5904–5924.
[73] E.E. Sickbert-Bennett, J.M. Samet, P.W. Clapp, H. Chen, J. Berntsen, K.L. Zeman, H. Tong, D.J. Weber, W.D. Bennett, Filtration efficiency of hospital face mask alternatives available for use during the COVID-19 pandemic, JAMA Intern. Med. 180 (12) (2020) 1607–1612.
[74] B. Sousa-Pinto, A.P. Fonte, A.A. Lopes, B. Oliveira, J.A. Fonseca, A. Costa-Pereira, O. Correia, Face masks for community use: an awareness call to the differences in materials, Respirology 25 (8) (2020) 894.
[75] T. Joo, M. Takeuchi, F. Liu, M.P. Rivera, J. Barr, E.S. Blum, E. Parker, J.H. Tipton, J. Varnedoe, B. Dutta, et al., Evaluation of particle filtration efficiency of commercially available materials for homemade face mask usage, Aerosol Sci. Technol. 55 (8) (2021) 930–942.
[76] A. Karakoç, E. Hiltunen, J. Paltakari, Geometrical and spatial effects on fiber network connectivity, Compos. Struct. 168 (2017) 335–344.
[77] E. Demirci, E. Sozumert, M. Acar, B. Pourdeyhimi, V. Silberschmidt, Developing 3d fully parametric multi-scale computational model for nonwoven simulations (2019).
[78] E. Sozumert, Y. Kiyak, E. Demirci, V.V. Silberschmidt, Effect of microstructure on porosity of random fibrous networks, J. Text. Inst. 111 (12) (2020) 1713–1723.
[79] A. Karakoc, J. Paltakari, E. Taciroglu, On the computational homogenization of three-dimensional fibrous materials, Compos. Struct. 242 (2020) 112151.
[80] M.A. Tahir, H. Vahedi Tafreshi, Influence of fiber orientation on the transverse permeability of fibrous media, Phys. Fluids 21 (8) (2009) 083604, doi:10.1063/1.3211192.
[81] A.K. Pradhan, D. Das, R. Chattopadhyay, S. Singh, Effect of 3d fiber orientation distribution on transverse air permeability of fibrous porous media, Powder Technol. 221 (2012) 101–104, doi:10.1016/j.powtec.2011.12.027. Selected papers from 2010 AIChE Annual Meeting
[82] S. Zobel, B. Maze, H. Vahedi Tafreshi, Q. Wang, B. Pourdeyhimi, Simulating permeability of 3-d calendered fibrous structures, Chem. Eng. Sci. 62 (22) (2007) 6285–6296, doi:10.1016/j.ces.2007.07.007.
[83] B. Borgelink, A. Carchia, J. Hernndez-Snchez, D. Caputo, J. Gardeniers, A. Susarrey-Arce, Filtering efficiency model that includes the statistical randomness of non-woven fiber layers in facemasks, Sep. Purif. Technol. 282 (2022) 120049, doi:10.1016/j.seppur.2021.120049.
[84] S. Ando, M. Nishikawa, M. Kaneda, K. Suga, Numerical simulation of filtration processes in the flow-induced deformation of fibrous porous media by a three--dimensional two-way fluid–structure interaction scheme, Chem. Eng. Sci. 252 (2022) 117500.
[85] O. Aydin, B. Emon, S. Cheng, L. Hong, L.P. Chamorro, M.T.A. Saif, Performance of fabrics for home-made masks against the spread of COVID-19 through droplets: a quantitative mechanistic study, Extreme Mech. Lett. 40 (2020) 100924.
[86] E. Tosta, Transmission of severe acute respiratory syndrome Coronavirus 2 through asymptomatic carriers and aerosols: a major public health challenge, Rev. Soc. Bras. Med. Trop. 53 (2020).
[87] B. Illes, P. Gordon, Filtering efficiency measurement of respirators by laser-based particle counting method, Measurement 176 (2021) 109173.
[88] F. Drewnick, J. Pikmann, F. Fachinger, L. Moormann, F. Sprang, S. Borrmann, Aerosol filtration efficiency of household materials for homemade face masks: influence of material properties, particle size, particle electrical charge, face velocity, and leaks, Aerosol Sci. Technol. 55 (1) (2021) 63–79.
[89] J. Payen, P. Vroman, M. Lewandowski, A. Perwuelz, S. Call-Chazelet, D. Thomas, Influence of fiber diameter, fiber combinations and solid volume fraction on air filtration properties in nonwovens, Text. Res. J. 82 (19) (2012) 1948–1959, doi:10.1177/0040517512449066.
[90] W. Li, S. Shen, H. Li, Study and optimization of the filtration performance of multi fiber filter, Adv. Powder Technol. 27 (2) (2016) 638–645, doi:10.1016/j.apt.2016.02.018.
[91] S. Adanur, A. Jayswal, Filtration mechanisms and manufacturing methods of face masks: an overview, J. Ind. Text. (2020), doi:10.1177/1528083720980169. 152808372098016
[92] Z. Zhang, D. Ji, H. He, S. Ramakrishna, Electrospun ultrafine fibers for advanced face masks, Mater. Sci. Eng. 143 (2021) 100594, doi:10.1016/j.mser.2020.100594.
[93] K. Wang, H. Zhao, The influence of fiber geometry and orientation angle on filtration performance, Aerosol Sci. Technol. 49 (2) (2015) 75–85, doi:10.1080/02786826.2014.1003278.
[94] X. Zhang, X. Jin, A comparison of filtration performance of triangular and circular cross-section fibre, Indian J. Fibre Text. Res. (2017) 7.
[95] J. Zhou, L. Zhang, B. Zhang, W. Gong, Study on filtration performance of elliptical fiber with different arrangements, J. Eng. Fiber Fabr. 15 (2020). 155892501989388